Numerical investigation of a 3D Hybrid High-Order Method for the Indefinite Time-Harmonic Maxwell Problem

Matteo Cicuttin, Christophe Geuzaine

Numerical investigation of a 3D Hybrid High-Order Method for the Indefinite Time-Harmonic Maxwell Problem

Matteo Cicuttin, Christophe Geuzaine

October 10, 2022

Abstract

Hybrid High-Order (HHO) methods are a recently developed class of methods belonging to the broader family of Discontinuous Sketetal methods. Other well known members of the same family are the well-established Hybridizable Discontinuous Galerkin (HDG) method and the Weak Galerkin (WG) method. HHO provides various valuable assets such as simple construction, support for fully-polyhedral meshes and arbitrary polynomial order, great computational efficiency, physical accuracy and straightforward support for *hp*-refinement. In this work we propose an HHO method for the indefinite time-harmonic Maxwell problem and we evaluate its numerical performance. In addition, we present the validation of the method in two different settings: a resonant cavity with only Dirichlet conditions and a parallel plate waveguide problem employing all the available boundary conditions. Finally, as a realistic application, we demonstrate HHO used on the study of the return loss in a waveguide mode converter.

1 Introduction

Discontinuous Galerkin (DG) methods are very successful discretization methods for the numerical solution of PDEs. Such discretizations rely on discrete spaces made out of broken polynomials, yielding discontinuous discrete solutions. Because of the nature of broken spaces however, DG methods tipically yield a number of degrees of freedom much higher than classical Finite Elements: this is frequently a source of criticism about DG. Hybrid methods were therefore introduced to mitigate this issue while retaining all the advantages typical of DG, like full polyhedral support and arbitrary polynomial order. The strategy behind hybrid methods is, very informally, to define some element-local problems and subsequently couple them via face unknowns only: in this way one obtains a global problem posed only in terms of face-based unknowns, contrary to DG which yields a global problem posed in terms of cell-based unknowns. Since unknowns of the global problem are face-based, this class of methods is also known as Discontinuous Skeletal (DS) methods.

An extremely successful DS method is the Hybridizable Discontinuous Galerkin (HDG) [21], which has been used in a multitude of contexts including magnetostatics [11] and electromagnetic wave propagation [33, 29, 32, 7, 30]. Roughly

speaking, the HDG discretization relies on a mixed formulation of the problem at hand, with the goal of approximating a triple including the primal variable, the dual variable and the trace of the primal variable on the skeleton of the mesh. Some form of static condensation is subsequently possible in order to obtain a global problem posed only on the skeleton of the mesh.

A more recent development in the family of Discontinuous Skeletal methods is the Hybrid High-Order method (HHO in the following) [25, 24]. The main features of HHO are the approximation of the solution with arbitrary order polynomials, support for fully polyhedral meshes and easy *hp*-refinement. In addition, HHO methods are constructed independently from the geometric dimension and the element shape, allowing fully generic implementations [16]. Contrary to HDG, HHO takes a purely primal viewpoint and places the unknowns both in the cells and on the faces of the mesh in order to approximate a pair including the primal variable in the cells and its trace on the skeleton. In particular, these unknowns are used by (i) a reconstruction operator, which reconstructs a high-order field in the cell and (ii) by a stabilization operator, which weakly enforces in each mesh cell the matching of the traces of the cell functions with the face unknowns. These two operators are then combined in a local bilinear form which, after local static condensation, is assembled into the global problem using the standard finite element procedure.

The different viewpoints taken by HDG and HHO are widely discussed in literature, we refer the reader to [21, 22, 25, 18] for the full details. Despite the very different viewpoints taken by the two methods, a remarkable result is that HDG and HHO can be bridged toghether in a common framework, as discussed in [20].

HHO methods have been used successfully in several fields of computational mechanics, for example solid mechanics [1, 2, 3], contact problems [9], obstacle problems [17] and fluid mechanics [8, 4]. Recent applications of HHO to acoustic time-domain wave problems can be found in [5] and [6]. To the best of our knowledge however, the only application to electromagnetics, and specifically to magnetostatics, is found in [10].

In this work we present a construction of an HHO method for the time-harmonic Maxwell problem, which adds to the family of polyhedral discretizations already successfully deployed on computational electromagnetics problems [33, 19]. As the time-harmonic Maxwell problem is notoriously hard to solve with iterative methods [15], direct solvers are frequently employed. Direct solvers however require huge amounts of memory, and for this reason efficient, high-order discretization techniques are of utmost importance. By employing skeletal (face-based) unknowns, hybrid methods are excellent candidates for this task.

2 Continuous setting

Let Ω be an open, simply connected subset of $\mathbb{R}^3$ (the method is suitable for any spatial dimension, we take $d = 3$ for conciseness). Standard notation will be used in the following, in particular $L^2(\Omega)$ denotes the Lebesgue space composed of the square integrable functions and $H(\mathrm{curl};\Omega)$ the space of those functions in $L^2(\Omega)$ whose curls are square-integrable. In addition, we denote as $H_0(\mathrm{curl};\Omega)$ the subspace of $H(\mathrm{curl};\Omega)$ composed of the functions of $H(\mathrm{curl};\Omega)$ whose trace

is zero on $\partial\Omega$. Finally, we denote with $(\cdot,\cdot)_{L^2(\Omega)}$ the inner product on $L^2(\Omega)$ and with $\|\cdot\|_{L^2(\Omega)}$ the corresponding norm.

We consider initially the time-harmonic problem with homogeneous Dirichlet boundary conditions

$$\begin{cases} \nabla\times(\mu^{-1}\nabla\times\boldsymbol{e}) - \omega^2\epsilon\boldsymbol{e} = \boldsymbol{f} & \text{in } \Omega \\ \hat{\boldsymbol{n}}\times\boldsymbol{e} = 0 & \text{on } \partial\Omega \end{cases}, \tag{1}$$

where ω is the angular frequency, μ, ϵ are piecewise constant material parameters, $\boldsymbol{e} \in \mathbb{C}^3$ is the unknown electric field and $\boldsymbol{f} := -i\omega\boldsymbol{j} \in \mathbb{C}^3$ is the divergence-free source current density. Problem (1) is readily translated in weak form: let $V := H_0(\mathrm{curl};\Omega)$; we seek $\boldsymbol{e} \in V$ such that

$$(\mu^{-1}\nabla\times\boldsymbol{e}, \nabla\times\boldsymbol{v})_{\mathbf{L}^2(\Omega)} - \omega^2(\epsilon\boldsymbol{e},\boldsymbol{v})_{\mathbf{L}^2(\Omega)} = (\boldsymbol{f},\boldsymbol{v})_{\mathbf{L}^2(\Omega)}, \quad \forall\boldsymbol{v}\in V. \tag{2}$$

3 Discrete setting

Let $\mathcal{M}(\mathcal{T},\mathcal{F})$ be a polyhedral mesh with $\#\mathcal{T}$ cells and $\#\mathcal{F}$ faces. A generic cell is denoted as $T \in \mathcal{T}$, whereas a generic face as $F \in \mathcal{F}$. Each cell T has diameter h_T and each face F has diameter h_F. The mesh size is defined as $h = \max_{T\in\mathcal{T}} h_T$. We attach to each element T a cell-based vector-valued polynomial $\mathbb{P}_3^k(T)$ and to each one of its n faces $F \in \partial T$ a face-based vector-valued polynomial $\mathbb{P}_2^k(F)$ of degree $k \geqslant 1$. Cell-based polynomials are 3-variate, have values in $\mathbb{C}^3$ and are evaluated directly in the physical element, whereas face-based polynomials have values in $\mathbb{C}^2$ tangent to the face itself. In particular, to define the polynomial space $\mathbb{P}_2^k(F)$ attached to a face F of the mesh, we introduce the affine mapping $\mathbf{T}_F : \mathbb{R}^2 \to H_F$, where H_F is the hyperplane in $\mathbb{R}^3$ supporting F. We subsequently set

$$\mathbb{P}_2^k(F) := \mathbb{P}_2^k \circ (\mathbf{T}_F^{-1})_{|F}.$$

We remark that an entirely similar procedure can be applied to evaluate face-based functions in the case $d = 2$ (the implementation details are available in [16]), in addition in that case the face-based polynomials will be scalar-valued. Generally speaking, the way in which we chose the face-based polynomial spaces allows to reflect at the discrete level the tangential continuity requirement that exists at the continuous level. By collecting the cell-based and face-based polynomials attached to an element, the element-local space of degrees of freedom is formed and denoted as

$$\mathsf{U}_T^k := \mathbb{P}_3^k(T) \times \left\{ \bigtimes_{F\in\partial T} \mathbb{P}_2^k(F) \right\}.$$

The elements of U_T^k are denoted as the pairs $\underline{\mathsf{u}}_T := (\mathsf{u}_T, \mathsf{u}_{\partial T})$. In turn, $\mathsf{u}_T \in \mathbb{P}_3^k(T)$ and $\mathsf{u}_{\partial T} = (\mathsf{u}_{F_1},\ldots,\mathsf{u}_{F_n}), \mathsf{u}_{F_i} \in \mathbb{P}_2^k(F_i)$ are the cell-based and the collection of face-based polynomials respectively (Figure 1). By collecting all the local polynomials attached to the mesh elements, the global discrete problem space is introduced as

$$\mathsf{U}_h^k := \left\{ \bigtimes_{T\in\mathcal{T}} \mathbb{P}_3^k(T) \right\} \times \left\{ \bigtimes_{F\in\mathcal{F}} \mathbb{P}_2^k(F) \right\},$$

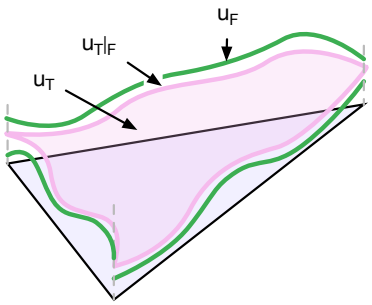

Figure 1: Visual representation of the *local* HHO space: to each mesh element we attach a cell-based function u_T and one face-based function u_F for each face F. Notice that on the vertices the face-based function are discontinuous.

where we remark that the face-based functions are single-valued (Figure 2). We will denote as $\underline{\mathsf{u}}_h \in \mathsf{U}_h^k$ the elements of the global discrete space and u_h the cell-based part of $\underline{\mathsf{u}}_h$. Homogeneous Dirichlet boundary conditions are enforced strongly by setting to zero the unknowns associated to the boundary faces by considering the subspace of U_h^k

$$\mathsf{U}_{h,0}^k := \left\{ \underline{\mathsf{u}}_h \in \mathsf{U}_h^k \mid \mathsf{u}_F = 0 \quad \forall F \in \partial\Omega \right\}.$$

Being the values of the face-based polynomials tangent to the faces of the elements, this naturally enforces $\hat{\boldsymbol{n}} \times \boldsymbol{e} = \boldsymbol{0}$. Lastly, we define the tangential trace on the face F as $\gamma_{t,F}(\boldsymbol{u}) := \hat{\boldsymbol{n}} \times (\boldsymbol{u} \times \hat{\boldsymbol{n}})$, with $\hat{\boldsymbol{n}}$ being the outward normal.

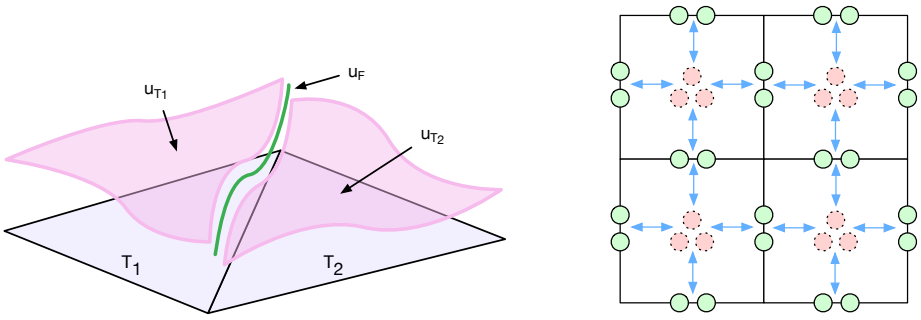

Figure 2: Visual representation of the *global* HHO space. On the left, the result of assemblying the local contributions; notice that the face-based functions are single-valued. On the right the HHO stencil, were we remark that the cell-based unknowns communicate via the face-based unknowns. Cell-based unknowns are eliminated locally via a Schur complement, so they do not appear in the global linear system.

3.1 The HHO operators

The general idea behind skeletal methods is to define some element-local problem which couples to the neighbouring elements via face-based unknowns only.

Subsequently, cell-based unknowns are eliminated locally via a Schur complement, allowing to obtain a global transmission problem posed in terms of face unknowns only.

In HHO, such local problems are built out of a *reconstruction operator* and a *stabilization* [24]. The reconstruction is typically derived from an integration by parts formula. In the present case we employ the well-known formula

$$(\nabla \times \boldsymbol{u}, \boldsymbol{v})_{\mathbf{L}^2(T)} = (\boldsymbol{u}, \nabla \times \boldsymbol{v})_{\mathbf{L}^2(T)} + (\boldsymbol{u}, \boldsymbol{v} \times \hat{\boldsymbol{n}})_{\mathbf{L}^2(\partial T)}, \tag{3}$$

to derive a *curl reconstruction* [10] operator $\mathcal{C} : \mathsf{U}_T^k \to \mathbb{P}_3^k(T)$. Informally speaking, on the right-hand side of (3) $\boldsymbol{u}$ is replaced with the cell-based function u_T in the first term and with the face-based functions $\mathsf{u}_{\partial T}$ in the second term. Having done these substitutions, the right-hand side must now depend from the newly introduced functions as

$$(\mathcal{C}\underline{\mathsf{u}}_T, \boldsymbol{v})_{\mathbf{L}^2(T)} := (\mathsf{u}_T, \nabla \times \boldsymbol{v})_{\mathbf{L}^2(T)} + \sum_{F \in \partial T} (\mathsf{u}_F, \boldsymbol{v} \times \hat{\boldsymbol{n}})_{\mathbf{L}^2(F)}, \quad \forall \boldsymbol{v} \in \mathbb{P}_3^k(T). \tag{4}$$

Equation (4) constitutes the definition of the *curl reconstruction operator* and the actual computation of $\mathcal{C}$ requires inverting a mass matrix in each element; this is done just once if a reference element is available (see [18, Chapter 8] for the implementation details).

Since $\mathcal{C}$ has a nontrivial kernel [18, Chapter 1], we also need a *stabilization* that penalizes the difference between the face-based functions $\mathsf{u}_{\partial T}$ and the tangential component of the cell-based function u_T on ∂T. This ultimately imposes weakly a tangential continuity requirement between elements. Let π_F^k be the standard face-based L^2-orthogonal projector, let also $\pi_{\gamma,F}^k = \pi_F^k \circ \gamma_{t,F}$. We employ a Lehrenfeld–Schöberl-like stabilization [18, 33] defined as

$$s_T(\underline{\mathsf{u}}_T, \underline{\mathsf{v}}_T) := \sum_{F \in \partial T} \zeta(\mathsf{u}_F - \pi_{\gamma,F}^k(\mathsf{u}_T), \mathsf{v}_F - \pi_{\gamma,F}^k(\mathsf{v}_T))_{\mathbf{L}^2(F)},$$

where $\zeta = \omega\sqrt{\epsilon/\mu}$ is a scaling factor chosen to have the correct units for the stabilization. A similar approach concerning the choice of the penalization parameter is taken in [33] in the HDG context.

Notice that the definitions of the reconstruction and the stabilization are *completely element-local*, and this feature will allow us to apply a local Schur complement and eliminate cell-based unknowns during assembly.

With this construction, we expect a convergence rate of $O(h^{k+1})$ for the L^2-norm of the error $\|\boldsymbol{e} - \mathsf{e}_h\|_{\mathbf{L}^2(\Omega)}$, where $\boldsymbol{e}$ is the solution of (1) and e_h is the cell-based component of its numerical approximation.

3.2 The discrete problem

In order to build the discrete problem we use the curl reconstruction to mimic locally the curl-curl term of (2). We collect this term alongside with the stabilization and the discrete equivalent of the mass term of (2) plus the right-hand side in the bilinear form $a_T : \mathsf{U}_T^k \times \mathsf{U}_T^k \to \mathbb{R}$ and linear form $l_T : \mathsf{U}_T^k \to \mathbb{R}$ as

$$\begin{aligned} a_T(\underline{\mathsf{e}}_T, \underline{\mathsf{v}}_T) &:= \mu^{-1}(\mathcal{C}\underline{\mathsf{e}}_T, \mathcal{C}\underline{\mathsf{v}}_T)_{\mathbf{L}^2(T)} + s_T(\underline{\mathsf{e}}_T, \underline{\mathsf{v}}_T) - \omega^2\epsilon((\mathsf{e}_T, 0), (\mathsf{v}_T, 0))_{\mathbf{L}^2(T)}, \\ l_T(\underline{\mathsf{v}}_T) &:= (\boldsymbol{f}, (\mathsf{v}_T, 0))_{\mathbf{L}^2(T)}, \end{aligned}$$

where the mass term $((\mathsf{e}_T,0),(\mathsf{v}_T,0))_{\mathbf{L}^2(T)}$ is purely cell-based and the source $\boldsymbol{f}$ is tested only against cell-based basis functions. Static condensation is applied locally to eliminate cell-based DOFs, we refer the reader to [16] for the details. The global problem is obtained by a standard finite element assembly of the bilinear form $a_h : \mathsf{U}_{h,0}^k \times \mathsf{U}_{h,0}^k \to \mathbb{R}$ and the linear form $l_h(\underline{\mathsf{v}}_h) : \mathsf{U}_{h,0}^k \to \mathbb{R}$

$$a_h(\underline{\mathsf{e}}_h, \underline{\mathsf{v}}_h) := \sum_{T\in\mathcal{T}} a_T(\mathsf{L}_T\underline{\mathsf{e}}_h, \mathsf{L}_T\underline{\mathsf{v}}_h),$$
$$l_h(\underline{\mathsf{v}}_h) := \sum_{T\in\mathcal{T}} l_T(\mathsf{L}_T\underline{\mathsf{v}}_h),$$

where L_T is the classical global-to-local face numbering mapping. We finally solve the global discrete problem of finding $\underline{\mathsf{e}}_h \in \mathsf{U}_{h,0}^k$ such that

$$a_h(\underline{\mathsf{e}}_h, \underline{\mathsf{v}}_h) = l_h(\underline{\mathsf{v}}_h) \quad \forall \underline{\mathsf{v}}_T \in \mathsf{U}_{h,0}^k.$$

3.3 Numerical validation

The described HHO method is implemented in the open-source numerical library DiSk++ (`https://github.com/wareHHOuse/diskpp`). The numerical validation was done on a resonant cavity problem in the domain $[0,1]^3$. The RHS is chosen to obtain the solution $\boldsymbol{e} = (0, 0, sin(\omega x)sin(\omega y))^T$ with $\omega = \pi$ and $\nu = \epsilon = 1$. The objective of the validation is to verify that the method converges with the expected rates and to assess its computational cost in comparison with a classical Symmetric Interior Penalty Discontinuous Galerkin (SIP-DG) discretization [27]. The linear systems obtained from the HHO and SIP-DG discretizations are solved using the PARDISO linear solver found in the Intel MKL library.

The convergence rates and the computational cost of the matrix factorization are summarized in Figure 3. The error convergence rate in L^2-norm results to be $O(h^{k+1})$, as expected. In addition, the computational cost of HHO results to be much lower than that of SIP-DG. Being HHO a skeletal discretization, the number of DOFs of the global system grows as $\mathcal{O}(\#\mathcal{F} \cdot k^{d-1})$, compared to $\mathcal{O}(\#\mathcal{T} \cdot k^d)$ in SIP-DG. As such, especially at high polynomial order and on meshes composed mainly of "standard" elements (tetrahedra or hexahedra), HHO is expected to perform much better than SIP-DG. Tables 1 and 2 provide additional confirmation to that expectation. Table 1 reports the number of operations done by PARDISO when deployed on the linear systems obtained from the discretization of the test problem with a tetrahedral mesh of 3072 elements. In Table 2, on the other hand, we report the computational advantage of HHO

Table 1: Computational cost comparison between HHO vs. SIP-DG on a tetrahedral mesh of 3072 elements.

	HHO		SIP-DG	
Degree	Memory	Mflops	Memory	Mflops
k=1	0.5 Gb	8.723	0.3 Gb	20.040
k=2	0.9 Gb	66.759	2.4 Gb	313.133
k=3	2.6 Gb	309.072	9.3 Gb	2.560.647

Table 2: Cost comparison between HHO vs. SIP-DG on a polyhedral mesh of 1210 elements (DBLS10 mesh of the FVCA6 benchmark).

	HHO		SIP-DG	
Degree	Memory	Mflops	Memory	Mflops
k=1	0.4 Gb	16.264	0.3 Gb	12.646
k=2	1.4 Gb	130.122	1.6 Gb	211.267
k=3	3.7 Gb	584.182	6.2 Gb	1.690.146
k=4	8.6 Gb	1.971.620	18.5 Gb	8.539.361

on the DBLS10 polyhedral mesh of the FVCA6 benchmark. As expected the HHO advantage, especially at low order, is slightly lower than in the tetrahedral case.

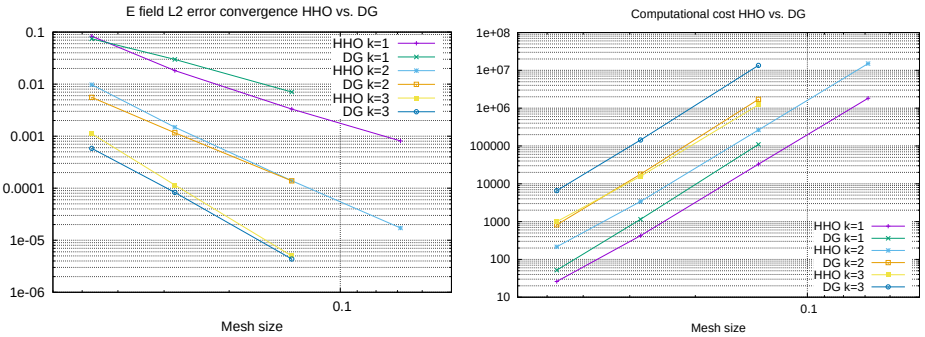

Figure 3: On the left panel, the L^2-norm convergence rates of HHO compared to Symmetric Interior Penalty Discontinuous Galerkin on tetrahedral meshes. On the right panel, the number of floating poing operations done by the linear solver. At high polynomial order, HHO is one order of magnitude cheaper than SIP-DG.

We conclude the computational performance evaluation with Table 3, in which we show the cost of HHO to attain a certain fixed error while varying mesh size and polynomial order.

Table 3: Computational effort required for HHO to attain roughly the same L^2-norm error at different polynomial orders.

Mesh h	k	Error	Mflops	DOFs	Memory
0.103843	2	3.56e-5	4089984	571392	11.7 Gb
0.207712	3	1.38e-5	309072	115200	2.6 Gb
0.415631	4	1.98e-5	16287	20160	0.5 Gb
0.832917	6	1.24e-5	1265	4032	0.1 Gb

4 Additional boundary conditions and field sources

Practical applications frequently require specialized treatment of boundaries and sources. In this section we discuss a plane wave boundary condition [12]

and a total field/scattered field decomposition. The former is basically a non-homogeneous Robin condition and is used either to impose an active plane wave source or a passive absorbing boundary condition on a boundary $\Gamma_Z \subset \partial\Omega$. The latter is a common technique to impose sources in the FDTD method and study reflection coefficients; it has been successfully used also in FETD (Finite-Element Time-Domain) [34] and other frequency domain methods [14, 31].

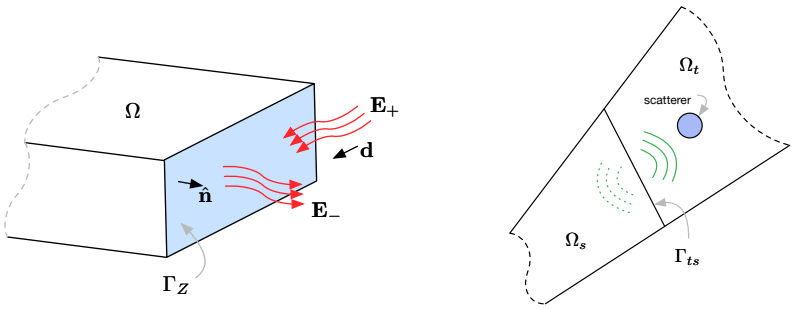

(a) (b)

Figure 4: In the left panel, the fields, vectors and surfaces involved in the definition of the plane wave boundary condition. In the right panel, the domains and interfaces involved in the TF/SF decomposition. On Ω_t the full field is computed, whereas in Ω_s only the reflections produced in Ω_t are computed.

4.1 Plane wave boundary condition

With reference to Figure 4a, let $\boldsymbol{E}_+$ denote the complex amplitude of the known electric field of a wavel entering Ω through Γ_Z and propagating in direction $\boldsymbol{d}$; similarly let $\boldsymbol{E}_-$ denote the complex amplitude of the unknown electric field of a wave exiting Ω through Γ_Z and propagating in direction $\hat{\boldsymbol{n}}$. In addition, let $\kappa^2 = \omega^2\mu\epsilon$. In this setting, the total electric field on Γ_Z at the point $\boldsymbol{x} \in \Gamma_Z$ is given by

$$\boldsymbol{e}(\boldsymbol{x}) = \boldsymbol{E}_+ e^{-i\kappa(\boldsymbol{d}\cdot\boldsymbol{x})} + \boldsymbol{E}_- e^{-i\kappa(\boldsymbol{n}\cdot\boldsymbol{x})}. \tag{5}$$

By taking the curl of (5) and applying the vector calculus identity $\nabla \times (\psi\boldsymbol{A}) = \psi(\nabla \times \boldsymbol{A}) + \nabla\psi \times \boldsymbol{A}$, we obtain

$$\nabla \times \boldsymbol{e} = -i\kappa \left(\boldsymbol{d} \times \boldsymbol{E}_+ e^{-i\kappa(\boldsymbol{d}\cdot\boldsymbol{x})} + \hat{\boldsymbol{n}} \times \boldsymbol{E}_- e^{-i\kappa(\hat{\boldsymbol{n}}\cdot\boldsymbol{x})} \right). \tag{6}$$

We now post-multiply by $\hat{\boldsymbol{n}}$ and replace (5) in the result to obtain

$$(\nabla \times \boldsymbol{e}) \times \hat{\boldsymbol{n}} + i\kappa\,(\hat{\boldsymbol{n}} \times (\boldsymbol{e} \times \hat{\boldsymbol{n}})) = i\kappa \left((\hat{\boldsymbol{n}} - \boldsymbol{d}) \times \boldsymbol{E}_+ e^{-i\kappa(\boldsymbol{d}\cdot\boldsymbol{x})} \right) \times \hat{\boldsymbol{n}}. \tag{7}$$

By pre-multiplying both sides of (7) by μ^{-1} we can make the wave admittance $Y = \sqrt{\epsilon/\mu}$ explicit

$$(\mu^{-1}\nabla \times \boldsymbol{e}) \times \hat{\boldsymbol{n}} + i\omega Y \boldsymbol{e}_t = i\omega Y \boldsymbol{e}_t^+(\boldsymbol{d}), \tag{8}$$

where we replaced the two double-cross-product terms of (7) with the shorthands $\boldsymbol{e}_t := \hat{\boldsymbol{n}} \times (\boldsymbol{e} \times \hat{\boldsymbol{n}})$ and $\boldsymbol{e}_t^+(\boldsymbol{d}) := \left((\hat{\boldsymbol{n}} - \boldsymbol{d}) \times \boldsymbol{E}_+ e^{-i\kappa(\boldsymbol{d}\cdot\boldsymbol{x})} \right) \times \hat{\boldsymbol{n}}$ respectively.

The condition just obtained goes under the name of *plane wave* condition. It can then be incorporated in the strong form Maxwell problem as

$$\begin{cases} \nabla \times (\mu^{-1}\nabla \times \boldsymbol{e}) - \omega^2 \epsilon \boldsymbol{e} = -i\omega \boldsymbol{j} & \text{in } \Omega \\ \hat{\boldsymbol{n}} \times \boldsymbol{e} = 0 & \text{on } \Gamma_D \\ (\mu^{-1}\nabla \times \boldsymbol{e}) \times \hat{\boldsymbol{n}} + i\omega Y \boldsymbol{e}_t = i\omega Y \boldsymbol{e}_t^+(\boldsymbol{d}) & \text{on } \Gamma_Z \end{cases}, \tag{9}$$

where $\boldsymbol{j}$ is the divergence-free current density, $\Gamma_Z \cup \Gamma_D = \partial\Omega$ and $\Gamma_Z \cap \Gamma_D = \varnothing$. Let $H_i(\mathrm{curl};\Omega)$ be the space defined as

$$H_i(\mathrm{curl};\Omega) := \{\boldsymbol{\phi} \in H(\mathrm{curl};\Omega) \mid \gamma_{t,\Gamma_Z}(\boldsymbol{\phi}) \in L^2(\Gamma_Z) \text{ on } \Gamma_Z, \hat{\boldsymbol{n}} \times \boldsymbol{\phi} = 0 \text{ on } \Gamma_D\}.$$

With standard manipulations, Problem (9) is translated to weak form, where we look for $\boldsymbol{e} \in H_i(\mathrm{curl};\Omega)$ such that the expression

$$\begin{aligned} \mu^{-1}(\nabla \times \boldsymbol{e}, \nabla \times \boldsymbol{v})_{\mathbf{L}^2(\Omega)} - \omega^2 \epsilon(\boldsymbol{e}, \boldsymbol{v})_{\mathbf{L}^2(\Omega)} + i\omega Y(\boldsymbol{e}_t, \boldsymbol{v})_{\mathbf{L}^2(\Gamma_Z)} = \\ = i\omega Y(\boldsymbol{e}_t^+(\boldsymbol{d}), \boldsymbol{v})_{\mathbf{L}^2(\Gamma_Z)} - i\omega(\boldsymbol{j}, \boldsymbol{v})_{\mathbf{L}^2(\Omega)}, \end{aligned} \tag{10}$$

holds for all the test functions $\boldsymbol{v} \in H_i(\mathrm{curl};\Omega)$. In the local HHO bilinear forms, the new impedance and boundary source terms appearing in (10) translate to a face-based mass matrix and a face-based right-hand side respectively, as in

$$\begin{aligned} a_T(\underline{\mathsf{e}}_T, \underline{\mathsf{v}}_T) &:= \mu^{-1}(\mathcal{C}\underline{\mathsf{e}}_T, \mathcal{C}\underline{\mathsf{v}}_T)_{\mathbf{L}^2(T)} + s_T(\underline{\mathsf{e}}_T, \underline{\mathsf{v}}_T) \\ &\quad - \omega^2 \epsilon((\mathsf{e}_T, 0), (\mathsf{v}_T, 0))_{\mathbf{L}^2(T)} \\ &\quad + \sum_{F \in \partial T} i\omega Y((0, \mathsf{u}_F), (0, \mathsf{v}_F))_{\mathbf{L}^2(\Gamma_Z)} \\ l_T(\underline{\mathsf{v}}_T) &:= \sum_{F \in \partial T} i\omega Y((0, \boldsymbol{e}_t^+(\boldsymbol{d})), (0, \mathsf{v}_F))_{\mathbf{L}^2(\Gamma_Z)} - i\omega(\boldsymbol{j}, (\mathsf{v}_T, 0))_{\mathbf{L}^2(T)} \end{aligned}$$

The global system assembly procedure remains identical to the previous case, except for the discrete global space of the problem, which is now

$$\mathsf{U}_{h,i}^k := \left\{\underline{\mathsf{u}}_h \in \mathsf{U}_h^k \mid \mathsf{u}_F = 0 \quad \forall F \in \Gamma_D\right\}.$$

4.2 Total field/scattered field decomposition

In a total/scattered field (TF/SF) decomposition the computational domain Ω is split in two partitions Ω_t and Ω_s such that $\Omega_t \cup \Omega_s = \Omega$, $\Omega_t \cap \Omega_s = \varnothing$ and $\overline{\Omega_t} \cap \overline{\Omega_s} = \Gamma_{ts}$ (Figure 4b). The field computed in Ω_s is then the result of the scatterings occurring in Ω_t minus the field due to the surface source applied on the interface Γ_{ts} or a subset of it. We refer the reader to [31, Section 3.2] for a detailed derivation of the TF/SF decomposition, here we limit ourselves to recall that in order to impose a surface source field $\boldsymbol{e}_{src}(\boldsymbol{x})$, $\boldsymbol{x} \in \Gamma_{ts}$ one can use the source term

$$\begin{aligned} \ell^{ts}(\boldsymbol{v}) := \mu^{-1}(\nabla \times \boldsymbol{e}_{src}, \nabla \times \boldsymbol{v})_{\mathbf{L}^2(\Omega_s)} - \omega^2 \epsilon(\boldsymbol{e}_{src}, \boldsymbol{v})_{\mathbf{L}^2(\Omega_s)} \\ - i\omega Y(\boldsymbol{e}_{src} \times \hat{\boldsymbol{n}}_{ts}, \boldsymbol{v})_{\mathbf{L}^2(\Gamma_{ts})} \end{aligned}, \tag{11}$$

where $\hat{\boldsymbol{n}}_{ts}$ is the normal vector on Γ_{ts} and pointing from Ω_t to Ω_s.

Let $\mathcal{I}_T^{ts}(\boldsymbol{u}) := (\boldsymbol{0}, \pi_{\gamma,F_1}^{k,ts}\boldsymbol{u}, \ldots, \pi_{\gamma,F_n}^{k,ts}\boldsymbol{u}) \in \mathsf{U}_T^k$, where $\pi_{\gamma,F_i}^{k,ts}\boldsymbol{u}$ returns the L^2 projection of $\boldsymbol{u}$ on F_i if $F_i \in \Gamma_{ts}$ and zero otherwise. The term (11) is readily translated to HHO as the element-local contribution to the right-hand side

$$\begin{aligned} l_T^{ts}(\underline{\mathsf{v}}_T) := \mu^{-1}(\mathcal{C}\mathcal{I}_T^{ts}(\boldsymbol{e}_{src}), \mathcal{C}\underline{\mathsf{v}}_T)_{\mathbf{L}^2(T)} + s_T(\mathcal{I}_T^{ts}(\boldsymbol{e}_{src}), \underline{\mathsf{v}}_T) \\ - i\omega Y(\mathcal{I}_T^{ts}(\boldsymbol{e}_{src}), \underline{\mathsf{v}}_T)_{\mathbf{L}^2(\Gamma_{ts})} \end{aligned}. \tag{12}$$

where T is an element that belongs to Ω_s and has at least one face in common with Γ_{ts}. Notice that since the cell part of $\mathcal{I}_T^{ts}(\boldsymbol{e}_{src})$ is zero, the discrete volumetric mass term vanishes.

5 Numerical validation of additional conditions and sources

In this section we provide some validation results about the impedance boundary condition and the total field/scattered field decomposition. To this aim, we set up a parallel-plate waveguide problem whose analytical solution can be readily obtained by basic transmission line theory considerations [23]. In particular, we will consider the propagation of an electromagnetic wave through a material discontinuity with various degrees of impedance mismatch. In this setting, we study the convergence to the analytical solution and the convergence of the return loss measured at the source.

5.1 Detailed validation setup

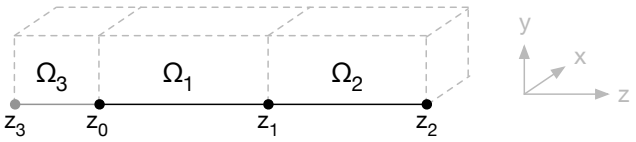

Figure 5: Computational domain used to setup a parallel-plate waveguide for the validation of the impedance boundary condition and the TF/SF decomposition.

Concretely, we consider the domain $\Omega = (0, 0.1) \times (0, 0.1) \times (-0.2, 2)$. Additionally, we subdivide Ω along the coordinate z in three subregions Ω_3, Ω_1 and Ω_2 (Figure 5). The region Ω_3 extends in the interval $(-0.2, 0)$ along z and is a scattered field region, whereas Ω_1 and Ω_2 are both total field region which cover the z intervals $(0, 1)$ and $(1, 2)$ respectively. On the boundaries parallel to the xz-plane a homogeneous Dirichlet boundary condition ($\hat{\boldsymbol{n}} \times \boldsymbol{e} = 0$) is applied, whereas on the boundaries parallel to the yz-plane a homogeneous Neumann boundary condition ($\hat{\boldsymbol{n}} \times \boldsymbol{h} = 0$) is applied. A plane wave source of amplitude $\boldsymbol{E}_0 = (0, 1, 0)^T$ is applied via (12) in the plane at $z = z_0 = 0$, whereas on the planes $z = z_3 = -0.2$ and $z = z_2 = 2$ an impedance boundary condition is imposed. In the regions Ω_3 and Ω_1 the material parameters are set to $\epsilon = \epsilon_0$ and $\mu = \mu_0$, simulating free space. On the other hand, in Ω_2 we set $\epsilon = \epsilon_r\epsilon_0$ and $\mu = \mu_0$ in order to obtain a material discontinuity on the plane at $z = z_1 = 1$. In turn, this gives on the same plane a reflection coefficient γ_{12} and a transmission coefficient τ_{12} (seen from 1 to 2).

In this setting, the reference solution can be defined piecewise by resorting to the standard transmission line theory (Figure 6). We start with Ω_1 by observing that there will be a forward wave due to the excitation at z_0, and a backward wave reflected by the material discontinuity at z_1. The expression of the forward wave is easily deduced to be $\boldsymbol{E}_0 e^{-i\kappa_1(z-z_0)}$; in addition we notice that at the point z_1 the phase is $\phi_1 = -i\kappa_1(z_1 - z_0)$. Subsequently, by using the last observation and the fact that at z_1 the reflection coefficient is γ_{12}, we deduce that the backward wave originating at z_1 can be written as $\boldsymbol{E}_0\,\gamma_{12}\,e^{i\kappa_1(z-z_1)}e^{\phi_1}$. Concerning Ω_2, as the domain is terminated by a matched impedance condition, we expect only a forward wave with initial amplitude $\boldsymbol{E}_0\,\tau_{12}$ and initial phase ϕ_1. Finally, as Ω_3 is a scattered field region, we expect to see only the backward wave originating at z_1, whose expression was already derived above. The complete, piecewise reference solution can finally be written as follows:

$$\boldsymbol{e}_{\text{ref}}(\boldsymbol{x}) = \begin{cases} \boldsymbol{E}_0\,\gamma_{12}\,e^{i\kappa_1(z-z_1)}e^{\phi_1} & \text{in } \Omega_3 \\ \boldsymbol{E}_0 e^{-i\kappa_1(z-z_0)} + \boldsymbol{E}_0\,\gamma_{12}\,e^{i\kappa_1(z-z_1)}e^{\phi_1} & \text{in } \Omega_1 \\ \boldsymbol{E}_0\,\tau_{12}\,e^{-i\kappa_2(z-z_1)}e^{\phi_1} & \text{in } \Omega_2 \end{cases} \tag{13}$$

5.2 Validation results

For the validation we consider three different situations: an almost matched situation, a situation with a moderate mismatch and one with a severe mismatch. In particular we will consider the values of ϵ_r in Ω_2 reported in Table 4. We recall [23] that the wave impedance in the domain Ω_i is computed from the material parameters as $Z_i = \sqrt{\epsilon/\mu}$. Given two differents, adjacent domains Ω_i and Ω_j, the reflection and transmission coefficients at the interface from Ω_i to Ω_j are computed as $\gamma_{ij} = \frac{Z_i - Z_j}{Z_i + Z_j}$ and $\tau_{ij} = 2\frac{Z_j}{Z_i + Z_j}$ respectively; the return loss in decibels at at the same interface is computed as $\text{RL(dB)} = 20\log_{10}|\gamma_{ij}|$ and the voltage standing wave ratio as $\text{VSWR} = \frac{1+|\gamma_{ij}|}{1-|\gamma_{ij}|}$. We recall that the return loss is given also by the ratio between the reflected and incident power at a given interface as $RL(dB) = 10\log_{10}(P_{\text{ref}}/P_{\text{fwd}})$. Finally, the power P flowing at a given interface Γ is obtained by evaluating the flux of the Poynting vector [28, Section 5.1] as $P = \int_\Gamma |\boldsymbol{e}|^2/Z d\Gamma$, where Z is the impedance of the domain adjacent to Γ.

Situation	ϵ_r	γ_{12}	τ_{12}	RL(dB)	VSWR
Almost matched	1.44	-1/11	10/11	-20.8279	1.2:1
Moderate mismatch	4	-1/3	2/3	-9.5424	2:1
Severe mismatch	64	-7/9	2/9	-2.1829	8:1

Table 4: The parameters of the three situations considered as validation cases. For a given value of ϵ_r, the analytical values of the reflection coefficient, transmission coefficient, return loss in dB and VSWR respectively are reported.

The results of the validation are reported in the Figures 7, 8 and 9. We considered polynomials degrees $k = 1$ (top row in the figures) and $k = 2$ (bottom row in the figures). In all cases the error decays with the expected rate ($\mathcal{O}(h^2)$ in the case $k = 1$ and $\mathcal{O}(h^3)$ in the case $k = 2$), see left column of Figures 7, 8 and

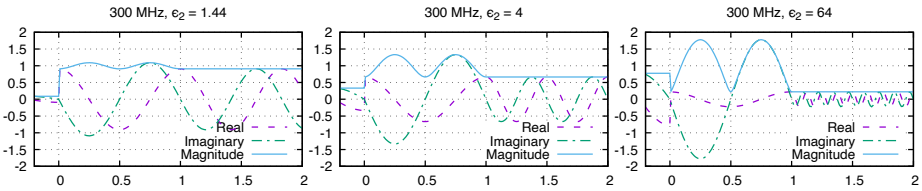

Figure 6: Analytical solution at 300 MHz in the three considered test cases. The symbol ϵ_2 denotes the relative permittivity in the subregion Ω_2 of the testing domain.

9. On the right column of the figures we reported the convergence of the return loss at the interface at z_0; we remark that this computation, especially in the severely mismatched situation, benefits greatly from higher order. In addition, we notice that there is no "direction" in the convergence of the value of the return loss: in some cases the convergence is from above, in some cases from below and in other cases there is an oscillation (getting smaller with smaller h) around the true value. This behaviour is in accordance with what was already observed in [13].

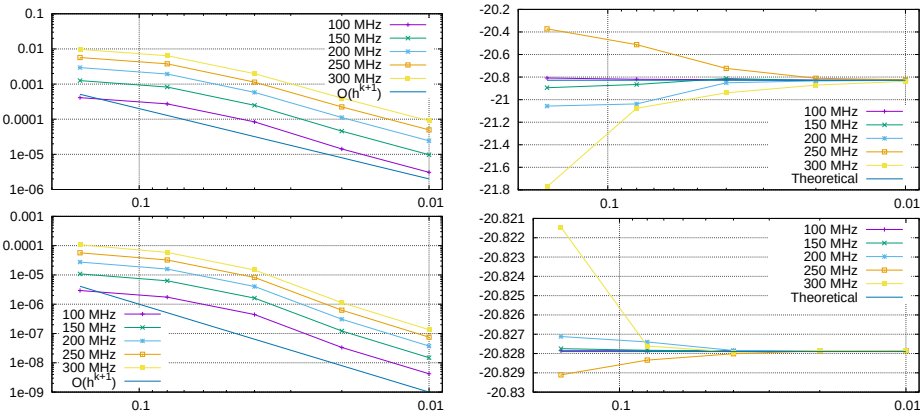

Figure 7: Almost matched (VSWR 1.2:1), on the top row polynomial order $k = 1$ and on the bottom row polynomial order $k = 2$. On the left column the convergence rate to the reference solution is reported, whereas in the right column the convergence of the return loss is depicted.

6 Study of a TE_{10} to TE_{20} mode converter

To conclude the numerical evaluation of the proposed HHO method, we consider a realistic test case of a waveguide mode converter. In this setting a waveguide is a hollow metallic pipe used to transport electromagnetic energy from a generator to a load (for example a transmitter and an antenna). Practical waveguides are tipically rectangular or circular and, as prescribed by the electromagnetic theory [23], the electromagnetic field inside a waveguide travels in discrete transverse modes indexed by integers m and n. A mode converter is a microwave device

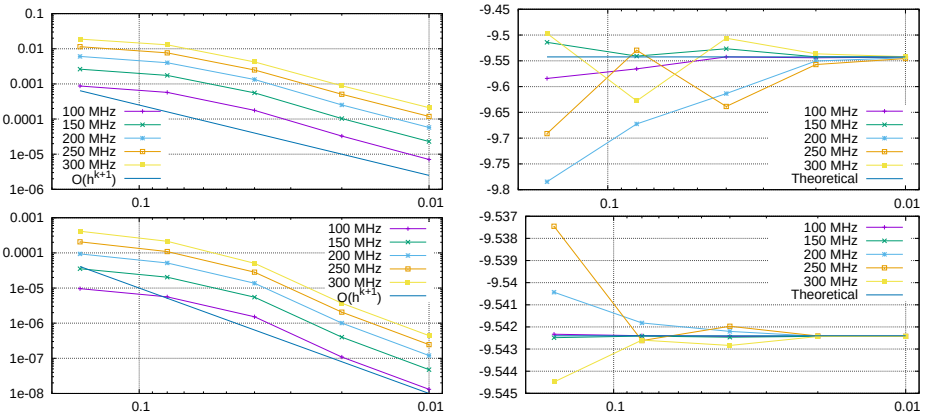

Figure 8: Moderate mismatch (VSWR 2:1), on the top row polynomial order $k = 1$ and on the bottom row polynomial order $k = 2$. On the left column the convergence rate to the reference solution is reported, whereas in the right column the convergence of the return loss is depicted.

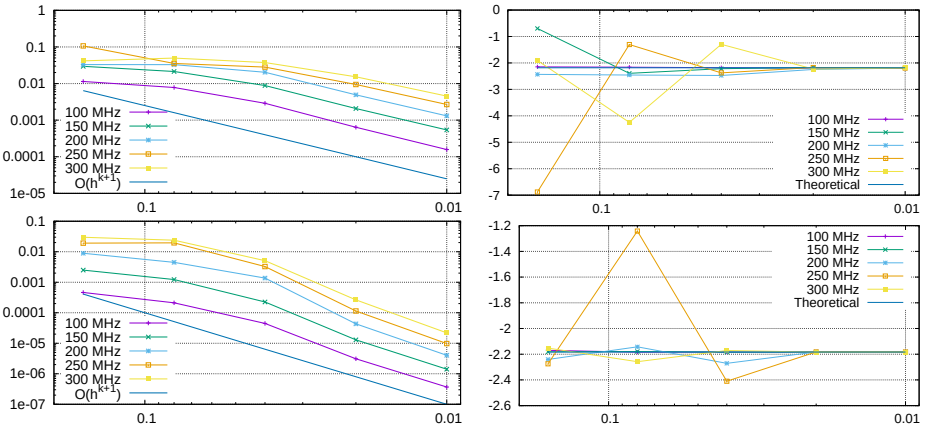

Figure 9: Severe mismatch (VSWR 8:1), on the top row polynomial order $k = 1$ and on the bottom row polynomial order $k = 2$. On the left column the convergence rate to the reference solution is reported, whereas in the right column the convergence of the return loss is depicted.

capable of changing the propation mode of a field in a waveguide, and can be used for example to split the power between two loads.

We consider a TE_{10} to TE_{20} waveguide mode converter of the type studied in [35, Chapter 14] and depicted in Figure 10. We are interested in determining

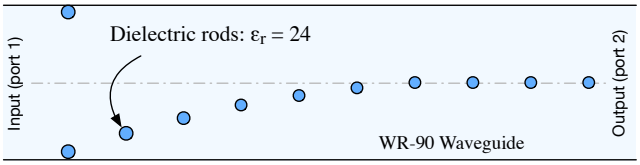

Figure 10: Structure of the simulated mode converter. The structure is built in a WR-90 waveguide and the dielectric rods (blue circles) have a relative permittivity $\epsilon_r = 24$. The input port is on the left (TE_{10} mode) and the output port is on the right (TE_{20} mode)

the TE_{10} reflection coefficient at the Port 1 (i.e. the S-parameter S_{11} [23]) of the structure in the frequency ranges between 7 and 11 GHz, where the mode conversion does not take place, and between 13 and 17 GHz, where mode conversion takes place (Figure 12). We compare our solution with the solution computed by a commercial multiphysics FEM package.

In the FEM model, the structure is terminated at both ends with Perfectly Matched Layers (PMLs) and excited with a waveguide port, as custom impedance boundary conditions are not available. On the other hand, in our HHO model we use an impedance boundary condition to terminate the structure. On the left side the impedance condition is matched to the wave impedance of the TE_{10} mode, whereas on the right side the termination is matched to the impedance of the output mode. The reason why we do not employ PMLs in our model is that their development requires a better understanding of the HHO behaviour when complex wavenumbers appear. Indeed, as observed also with the HDG method [26], HHO too appears to break down in this setting. To the best of our knowledge however, the HDG receipt [26] seems to not be straightforwardly applicable to HHO, therefore more investigation (which we will leave for a future contribution) is needed in this area.

The FEM mesh is composed of tetrahedral elements, whereas the HHO mesh is composed – in order to put in evidence the polyhedral nature of HHO – by a single layer of triangular prisms. In both the FEM and HHO models the amplitude of the reflected field is evaluated by exploiting the orthogonality between modes [28, Section 5.1.3] as

$$a_{\mathrm{TE}_{10}} := \frac{\int_\Gamma (\boldsymbol{e} - \boldsymbol{e}_{10}) \cdot \boldsymbol{e}_{10} \, \mathrm{d}\Gamma}{\int_\Gamma \boldsymbol{e}_{10} \cdot \boldsymbol{e}_{10} \, \mathrm{d}\Gamma}, \tag{14}$$

where Γ is the interface corresponding to Port 1 (Figure 10), $\boldsymbol{e}$ is the computed total field on Γ and $\boldsymbol{e}_{10}$ is the excitation applied on Γ. The amplitude is then used to compute the return loss S_{11} in decibels (Figure 11). In both regimes we observe a good match between the FEM solution and the HHO solution; the slight differences, negligible in practice, can be attributed to the slightly different models we employed.

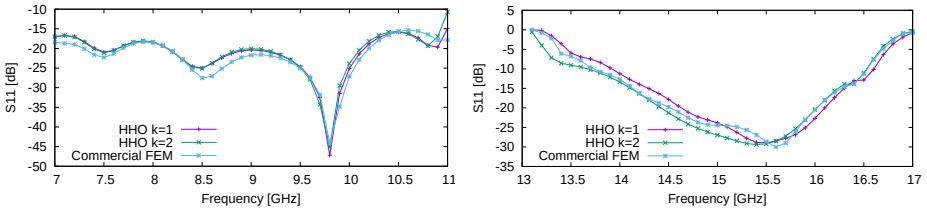

Figure 11: On the left the computed return loss between 7 and 11 GHz, where the mode conversion does not take place. On the right the computed return loss as TE_{10} mode between 13 and 17 GHz, where a TE_{10} to TE_{20} mode conversion takes place.

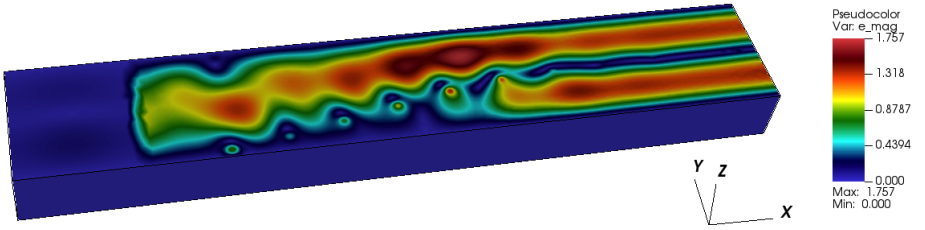

Figure 12: Field pattern at 15.5 GHz. From the left to right one can observe the scattered field region, the TF/SF transition where the excitation is applied and the total field region, where the mode conversion takes place. The left end is terminated with the impedance of the TE_{10} mode, whereas right end is terminated with the impedance of the TE_{20} mode.

7 Conclusions

We introduced a numerical method for the indefinite time-harmonic Maxwell problem inspired on the design philosophy of the original HHO method for elliptic problems, and we evaluated experimentally its computational performance against the classical SIP-DG method. As expected from hybrid methods, HHO requires far less computational effort than SIP-DG, which is an important advantage on the considered problem. More importantly, HHO also helps in reducing the quantity of memory required by the linear solver when compared to SIP-DG.

Subsequently we described the HHO realization of two important tools, namely a plane wave boundary condition and a total field/scattered field decomposition, which we validated obtaining the expected convergence of the considered quantities.

As a more real-world problem, we presented the study of a waveguide mode converter and we compared our results with those obtained from a commercial code. Satisfactory agreement was found.

There are many aspects of the method that still need to be understood, we leave deeper theoretical studies, as well as the introduction of other important numerical tools such as the PMLs, for a future contribution.

8 Acknowledgements

The authors wish to express their gratitude to S. Lemaire (INRIA), Z. Dong (INRIA) and T. Chaumont-Frelet (INRIA) for the useful discussions about some of the theoretical aspects of the HHO method.

References

[1] M. Abbas, A. Ern, and N. Pignet. Hybrid High-Order methods for finite deformations of hyperelastic materials. *Comput. Mech.*, 62(4):909–928, 2018.

[2] M. Abbas, A. Ern, and N. Pignet. A Hybrid High-Order method for incremental associative plasticity with small deformations. *Comput. Methods Appl. Mech. Engrg.*, 346:891–912, 2019.

[3] M. Abbas, A. Ern, and N. Pignet. A Hybrid High-Order method for finite elastoplastic deformations within a logarithmic strain framework. *Internat. J. Numer. Methods Engrg.*, 120(3):303–327, 2019.

[4] E. Burman, G. Delay, and A. Ern. An unfitted hybrid high-order method for the Stokes interface problem. *IMA J. Numer. Anal.*, 2021. hal-02280426.

[5] E. Burman, O. Duran, and A. Ern. Hybrid high-order methods for the acoustic wave equation in the time domain. *Commun. Appl. Math. Comput.*, 2021. hal-02922702.

[6] E. Burman, O. Duran, A. Ern, and M. Steins. Convergence analysis of hybrid high-order methods for the wave equation. *J. Sci. Comput.*, 87(3):Paper No. 91, 30, 2021.

[7] L. Camargo, B. López-Rodríguez, M. Osorio, and M. Solano. An HDG method for Maxwell's equations in heterogeneous media. *Computer Methods in Applied Mechanics and Engineering*, 368:113178, 2020.

[8] K. L. Cascavita, J. Bleyer, X. Chateau, and A. Ern. Hybrid discretization methods with adaptive yield surface detection for Bingham pipe flows. *J. Sci. Comput.*, 77(3):1424–1443, 2018.

[9] K. L. Cascavita, F. Chouly, and A. Ern. Hybrid high-order discretizations combined with Nitsche's method for Dirichlet and Signorini boundary conditions. *IMA J. Numer. Anal.*, 40(4):2189–2226, 2020.

[10] F. Chave, D. A. Di Pietro, and S. Lemaire. A discrete Weber inequality on three-dimensional hybrid spaces with application to the HHO approximation of magnetostatics. *Mathematical Models and Methods in Applied Sciences*, 32(01):175–207, 2022.

[11] Huangxin Chen, Weifeng Qiu, Ke Shi, and Manuel Solano. A Superconvergent HDG Method for the Maxwell Equations. *Journal of Scientific Computing*, 70(3):1010–1029, 2017.

[12] S. Chialina, M. Cicuttin, L. Codecasa, R. Specogna, and F. Trevisan. Plane wave excitation for frequency domain electromagnetic problems by means of impedance boundary condition. *IEEE Trans. Magn*, 51(3), 2015.

[13] M. Cicuttin, L. Codecasa, R. Specogna, and F. Trevisan. Complementary Discrete Geometric h -Field Formulation for Wave Propagation Problems. *IEEE Transactions on Magnetics*, 52(3):1–4, 2016.

[14] M. Cicuttin, L. Codecasa, R. Specogna, and F. Trevisan. Excitation by Scattering/Total Field Decomposition and Uniaxial PML in the Geometric Formulation. *IEEE Trans. Magn*, 52(3), 2016.

[15] M. Cicuttin, L. Codecasa, R. Specogna, and F. Trevisan. A geometric frequency-domain wave propagation formulation for fast convergence of iterative solvers. *IEEE Trans. Magn*, 53(6), 2017.

[16] M. Cicuttin, D. A. Di Pietro, and A. Ern. Implementation of Discontinuous Skeletal methods on arbitrary-dimensional, polytopal meshes using generic programming. *J. Comput. Appl. Math.*, 344:852–874, 2018.

[17] M. Cicuttin, A. Ern, and T. Gudi. Hybrid high-order methods for the elliptic obstacle problem. *J. Sci. Comput.*, 83(1):Paper No. 8, 18, 2020.

[18] M. Cicuttin, A. Ern, and N. Pignet. *Hybrid High-Order Methods. A primer with applications to Solid Mechanics*. SpringerBriefs in Mathematics. Springer, 2021.

[19] M. Cicuttin, R. Specogna, and F. Trevisan. Adaptivity based on the constitutive error for the Maxwell's eigenvalue problem on polyhedral meshes. *IEEE Trans. Magn*, 53(6), 2017.

[20] B. Cockburn, D. A. Di Pietro, and A. Ern. Bridging the Hybrid High-Order and Hybridizable Discontinuous Galerkin Methods. *ESAIM: Mathematical Modelling and Numerical Analysis*, 50, 2015.

[21] B. Cockburn, J. Gopalakrishnan, and R. Lazarov. Unified hybridization of discontinuous Galerkin, mixed, and continuous Galerkin methods for second order elliptic problems. *SIAM J. Numer. Anal.*, 47(2):1319–1365, 2009.

[22] B. Cockburn, J. Gopalakrishnan, and F.-J. Sayas. A projection-based error analysis of HDG methods. *Math. Comp.*, 79(271):1351–1367, 2010.

[23] R. E. Collin. *Foundations for Microwave Engineering*. Wiley, 2001.

[24] D. A. Di Pietro and A. Ern. A Hybrid High-Order locking-free method for linear elasticity on general meshes. *Comput. Meth. Appl. Mech. Engrg.*, 283:1–21, 2015.

[25] D. A. Di Pietro, A. Ern, and S. Lemaire. An arbitrary-order and compact-stencil discretization of diffusion on general meshes based on local reconstruction operators. *Comput. Meth. Appl. Math.*, 14(4):461–472, 2014.

[26] J. Gopalakrishnan, S. Lanteri, N. Olivares, and R. Perrussel. Stabilization in relation to wavenumber in HDG methods. *Advanced Modeling and Simulation in Engineering Sciences*, 2, 2015.

[27] P. Houston, I. Perugia, A. Schneebeli, and D. Schoetzau. Interior penalty method for the indefinite time-harmonic Maxwell equations. *Numerische Mathematik*, 100:485–518, 2005.

[28] J. Jin and D. J. Riley. *Finite Element Analysis of Antennas and Arrays*. Wiley, 2009.

[29] L. Li, S. Lanteri, N. Asger Mortensen, and M. Wubs. A hybridizable discontinuous Galerkin method for solving nonlocal optical response models. *Computer Physics Communications*, 219:99–107, 2017.

[30] L. Li, S. Lanteri, and R. Perrussel. Numerical investigation of a high order hybridizable discontinuous galerkin method for 2d time-harmonic maxwell's equations. *COMPEL - The international journal for computation and mathematics in electrical and electronic engineering*, 32, 2013.

[31] R. G. Marchand, M. M. Botha, and D. B. Davidson. Total and Scattered Field Decomposition for the Vector Helmoholtz Equation Using the FETI. *Electromagnetics*, 28:77–91, 2008.

[32] G. Nehmetallah, S. Lanteri, S. Descombes, and A. Christophe. An Explicit Hybridizable Discontinuous Galerkin Method for the 3D Time-Domain Maxwell Equations. In Spencer J. Sherwin, David Moxey, Joaquim Peiró, Peter E. Vincent, and Christoph Schwab, editors, *Spectral and High Order Methods for Partial Differential Equations ICOSAHOM 2018*, pages 513–523, Cham, 2020. Springer International Publishing.

[33] N.C. Nguyen, J. Peraire, and B. Cockburn. Hybridizable discontinuous Galerkin methods for the time-harmonic Maxwell's equations. *Journal of Computational Physics*, 230(19):7151–7175, 2011.

[34] D. J. Riley, J. Jin, Z. Lou, and L. E. R. Petersson. Total-and Scattered-Field Decomposition Technique for the Finite-Element Time-domain Method. *IEEE Trans. Ant. Prop*, 54(1), 2006.

[35] V. Zhurbenko, editor. *Electromagnetic Waves*. InTech, Rijeka, Croatia, 2011.